Nanoscale

Accepted Manuscript

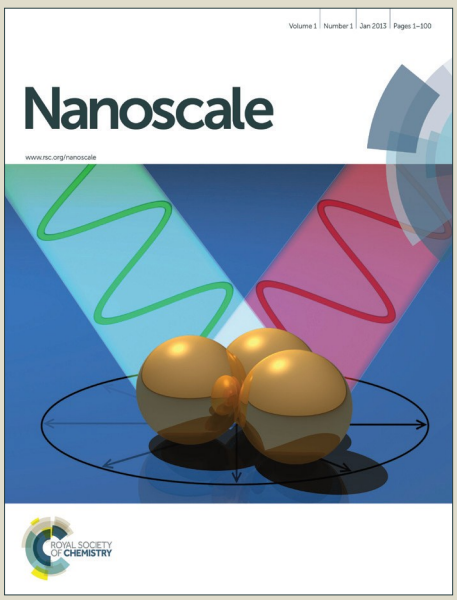

ROYAL SOCIETY OF CHEMISTRY

www.rsc.org/nanoscale

Nanoscale

RSCPublishing

ARTICLE

Local pH Tracking in Living Cells

Cite this: DOI: 10.1039/x0xx00000x

Chieh-Jui Tsou,[a†] Chih-Hao Hsia,[b†] Jia-Yin Chu,[a] Yann Hung,[a] Yi-Ping Chen,[b] Fan-Ching Chien,[c] Keng C. Chou,[d] Peilin Chen[b, *] and Chung-Yuan Mou[a, *]

Received ooth January 2012,
Accepted ooth January 2012

DOI: 10.1039/x0xx00000x

www.rsc.org/

Continuous and simultaneous 3D single-particle movement and local pH detection in HeLa cells was demonstrated for the first time by combining fluorescent mesoporous silica nanoparticles (FMSNs) and a single-particle tracking (SPT) technique with a precision of ~10 nm. FMSNs, synthesized by the co-condensation of both pH-sensitive and reference dyes with a silica/surfactant source, allow long-term reliable ratiometric pH measurements with precision better than 0.3 pH unit because of their excellent brightness and stability. The pH variation in the surrounding area of FMSNs during endocytosis was monitored in real-time. Acidification and low mobility of FMSNs was observed at the early endocytic stage, whereas basification and high mobility of FMSNs was observed at the late stage. Our results indicate that it is possible to monitor local pH changes in the environments surrounding nanoparticles during the cellular uptake process of FMSNs, which provides much needed information for designing an efficient drug delivery nanosystem.

Introduction

Effectiveness of nanomedicines highly depends on the development of the nanocarriers that can selectively and efficiently deliver the gene or therapeutic agents to the targeted cells with minimal toxicity. It has been shown that various nanoparticles (NPs) can be used as nanocarriers for controlled release applications.[1, 2] Among these NPs, mesoporous silica nanoparticles (MSNs) have attracted a lot of attention in recent years because of their controllable structure, high surface area, good bio-compatibility, and ease of surface modification.[3] MSNs have been proven to be a versatile platform for diagnosis and therapeutics through incorporation of multifunctional agents.[4] MSNs can simultaneously carry fluorescence,[5] magnetic agents,[6] drugs and biomolecules.[7] These excellent properties of MSNs have been broadly demonstrated in the biomedical applications.

Studies on the cellular uptake of NPs have shown that the processes depend on their sizes, shapes, and surfaces.[8,9] With different sizes and functionalized surfaces, NPs can travel through living cells in many different ways which result in different fates. To date, most studies of the interaction between NPs and cells have been focused on the entry and the final destination.[10] Fluorescence microscopy is often used to observe the locations of the NPs in fixed cells.[11] However, successful applications of NPs for nanomedicine require a deeper knowledge of the entire intracellular itinerary with information about their local environments. It is essential to study the pathway of a single particle, instead of the ensemble average, in order to observe important but rare events,[12] and to correlate the local chemical environment with the particle's pathway.

An efficient delivery of NPs to a targeted destination in a cell needs to overcome many barriers with unspecific attractive or steric repulsive interactions.[13] To exert the intended function of nanocarriers, various surface functionalizations of nanocarriers have been used to overcome barriers.[14-16] An example is the use of polycationic polyethylenimine (PEI) for endosomal escape.[17, 18] However, a detailed understanding of the nanocarriers' pathways and interactions with the local environment is still missing. The information is crucial for designing a better functionalized nanocarrier. Since the transportation of nanocarriers following the endocytosis is associated with changes of environmental pH,[19] building a local pH sensor using a trackable nanocarrier appears to be a desirable approach.

To track the positions of the nanocarriers, fluorescence microscopy is a powerful and commonly used tool. Recently, various nanomaterials have been successfully applied in intracellular pH sensing with a high signal-to-noise ratio and low cellular toxicity.[20-25] For a broad application, the criteria of a good optical nanosensor should include accessibility, sensitivity, photo-stability and a well-controlled structure. Dye-loaded fluorescent mesoporous silica nanoparticles (FMSNs)[26-28] are good optical nanosensors,[29] because they satisfy the aforementioned criteria and can be multi-functional carriers for drugs and enzymes.[30] The ratiometric fluorescence method has been recently employed extensively to collect reliable information by avoiding the interference from fluctuations of the light source and the concentration of the optical probes.[23, 26, 31] Common ratiometric pH sensing is built upon the emission intensity ratio (EIR) contributed from two disparate dyes (pH-sensitive and pH-insensitive dyes).[32, 33] The fluorescent ratiometric pH sensors have been applied in intracellular imaging[20,

†: Equal contribution
a. Department of Chemistry, National Taiwan University, Taipei, Taiwan 106
b. Research Center for Applied Sciences, Academia Sinica, Taipei, Taiwan 115
c. Department of Optics and Photonics, National Central University, Chung-Li, Taiwan 320
d. Department of Chemistry, University of British Columbia, Vancouver, BC V6T 1Z1 Canada
*corresponding authors: cymou@ntu.edu.tw (Chung-Yuan Mou); peilin@gate.sinica.edu.tw (Peilin Chen)
Electronic Supplementary Information (ESI) available: Experimental details, characterization data, control experiments, details of single-particle tracking studies and statistics are in the supporting information. See DOI: 10.1039/b000000x/

[25] and specific organelle targeting,[22] which were mostly observed using confocal microscopy. However, images of an ensemble of nanosensors in a selected intracellular area could not reveal the details of how the pH changed around a single particle throughout its trajectory. Therefore, 3D single-particles tracking (SPT) is needed for monitoring the environment around a single particle. 3D-SPT[34] has been applied to visualize membrane dynamics,[35] following protein trafficing in live cells,[36] evaluating the local transportation speed within the cell,[37] and the early stage of cellular uptake of nanoparticles.[11] Two common 3D-SPT methods are categorized into active feedback-based methods[36-40] or wide field imaging based tracking techniques[41-45]. The former method is a sophisticated technique equipped with active feedback in x-y-z directions using a fast 3D translational stage, but it is costly and can only track on a single target at a given time. In contrast, the latter technique allows multiple probes be detected simultaneously, unless the emitters diffuse out of the stationary detection region (approximately 1 μm in the z-axis around the focal plane). In addition, the later technique is commonly used for 3D super-resolution imaging, such as Stochastic Optical Reconstruction Microscopy (STORM).[44] Considering the potential of its widespread applications, 3D-SPT was chosen to track a single FMSN in 3D and to monitor pH changes.

In this work, MSNs equipped with ratiometric pH sensing for fluorescent imaging were prepared by co-conjugating a pH sensitive dye, fluorescein isothiocyanate (FITC), and a reference dye, rhodamine B isothiocyanate (RITC), (named as FMSNs). Due to their nanosize and excellent fluorescence intensity, FMSNs can be easily tracked by a 3D-SPT system. We demonstrated simultaneous detection of the 3D trajectory of FMSNs and the local pH in a HeLa cell during the endocytic process where the pH variation during the transportation of single nanoparticles between the cytoplasm and endosomes was monitored.[46] The information is crucial for controlling the pathway of the nanoparticles[47] or overcoming intracellular barriers[48] in the use of drug delivery nanoparticles.

Experimental

Materials

Cetyltrimethylammonium bromide (CTAB, 99%+), tetraethyl orthosilicate (TEOS, 98%), aminopropryltrimethoxysilane (APTMS, 95%), fluorescein isothiocyanate (FITC, 90%), disodium hydrogen phosphate (99%), sodium dihydrogen phosphate (99%) and methyl viologen hydrate (Paraquat, 98%) were obtained from Acros Organics. Ammonia hydroxide (35 wt%) and ethanol (99%) were purchased from Fisher Scientific. Ammonium nitrate (99%) and rhodamine B isothiocyanate (RITC, 70+%) were obtained from Sigma-Aldrich. N-trimethoxysilypropyl-N,N,N-trimethylammonium chloride (TA, 50%) and 3-trihydroxysilypropylmethylphosphonate, sodium salt (THPMP, 42%) were purchased from GELEST. N-(3-triethylammoniumpropyl)-4- (6-(4-diethylamino)phenyl)hexatrienyl) pyridinium dibromide (FM-4-64, 99%) was purchased from Invitrogen. All reagents were used as received.

Preparation of Dye Conjugated APTMS

To prepare the FITC-conjugated APTMS and RITC-conjugated APTMS, we followed the previously reported procedure developed in our laboratory.[28] The amine-reactive isothiocyanate group on FITC or RITC was utilized to form a covalent bond with the amine group on APTMS. FITC-conjugated and RITC-conjugated APTMS were prepared freshly before use. 6 mg of FITC was dissolved in 15 mL of ethanol, and 180 μL of APTMS was added into the FITC solution. The mixture was stirred in the dark overnight. RITC-APTMS was prepared by following the same procedure, but using one-third of the amount.

Synthesis of FMSNs(+)

Fluorescently labeled mesoporous silica nanoparticles (FMSNs) were prepared by conjugating both FITC and RITC onto the MSNs through ATPMS during the growth of the MSNs. Initially, 0.29 g of CTAB was dissolved in 150 g of a 0.51 M ammonium hydroxide water solution, and then 2.5 mL of a 0.41 M TEOS ethanol solution was added. The mixture was sealed in a flask with parafilm and heated to 40 ℃ under continuous stirring. After 4-hours of stirring, the parafilm on the flask was removed, then 8.1 mL of the APTMS-conjugated FITC ethanol solution and 3.4 mL of a 0.89 M TEOS ethanol solution were sequentially added into the mixture. After stirring for one hour, 0.54 mL of APTMS-conjugated RITC ethanol solution was then added, and then the mixture was stirred for another hour. After the mixture was aged at 40 ℃ without stirring for 24 hours, the pH value of the solution was altered to 10 by adding ammonium, and then 400 μL of TA was added. The mixture was sealed in flask again and heated to 40 ℃ under continuous stirring for 2 hours. The resulting product was washed by two routines to remove the surfactant template and unwanted physical absorbed chemicals. Routine 1: The resulting product (FMSNs(+)) were collected and dispersed in 25 mL of ethanol with sonication and then centrifuged to collect the precipitated product. Routine 2: The precipitated product was dispersed in the ammonium nitrate/ ethanol solution (6 g/ 50 mL) and stirred at 60 ℃ for one hour. First, Routine 1 was performed four times, and then Routine 2 was performed once. Second, Routine 1 was performed three times, and then Routine 2 once more using only half the amount of ammonium nitrate (3 g/ 50 mL). Finally, Routine 1 was repeated three more times, and the resulting FMSNs(+) were stored in 99.5% ethanol in the dark.

Property Characterization of FMSNs(+)

Particle sizes were measured on a transmission electron microscope (TEM) (Hitachi H-7100) operated at 100 kV. TEM samples were prepared by depositing a drop of diluted FMSN in ethanol solution on a carbon-coated Cu grid and dried in air. A N_2 adsorption-desorption isotherm was determined on a Micrometric ASAP 2010 apparatus at 77 K under continuous adsorption conditions. The sample was then degassed at 10^{-3} Torr at 110 °C for 16 hours prior to the experiments. The pore volume and pore size distribution plots were obtained from the analysis of the adsorption or desorption isotherm using the BJH (Barrett–Joyner–Halenda) method. The surface area was obtained by BET (Brunauer – Emmett – Teller) analysis. The fluorescent spectrum was collected from FMSN(+) aqueous solution, achieved by centrifugation and solvent replacement, excited by 473-nm light in a PMMA cuvette using a Hitachi F-4500 fluorescence spectrophotometer. The powder X-ray diffraction pattern was recorded using a PANalytical, X'per PRO diffractometer with the Cu Kα radiation (λ = 1.5418 Å), 2θ = 0.5°-8°. The dynamic light scattering and Zeta potential of FMSNs in aqueous solution were obtained with a Malvern Zetasizer Nano ZS. The hydrodynamic diameters of the FMSNs(+) were calculated by Stokes-Einstein equation. The detection mode for Zeta potential is noninvasive backscatter and the detection angle is 17°. The schematic and characterization of FMSNs(+) are shown in figure 1.

Fluorescence microscope setup

Simultaneous 3D single FMSN tracking and pH sensing were achieved by combining a wide-field imaging based single-particle tracking technique and FRET fluorescence microscopy. The schematic setup is shown in Figure 2. The setup was built upon an inverted fluorescence microscope (IX71, Olympus) with an oil objective lens (PlanApo N 60X, NA 1.42, Olympus). The image was collected by a camera (SSC-DC393, Sony). To limit sample drift, the

sample holder was immobilized on a homemade stage, and a built-in fine adjustment locker (manual controller, Olympus) was employed in the focusing system in order to lock the stage of the objective lens while performing the single particle tracking. To obtain fluorescence images of the FMSNs, the samples were excited with a 473-nm laser. The dual-color fluorescence image was collected by a CMOS camera (Neo sCMOS DC-152Q-C00-FI, Andor) using Andor software. A FRET split imaging system (Olympus) was installed in front of the camera to separate the fluorescent signals form FITC and RITC for ratiometric pH sensing. The dichroic mirror (550-nm long pass) in the FRET split imaging system was custom-made by Chroma.The signal passed through a single-band bandpass filter (520/35 nm or 593/46 nm, Semrock) for further background suppression. Between the FRET split imaging system and the camera, a cylindrical lens (f = 30 cm) was inserted to introduce astigmatism for depth (z-axis) localization.

Z-Axial Position Calibration

3D single-particle tracking is achieved using an astigmatism imaging method.[11,41,42] The cylindrical lens introduces slightly different focal length in the x and y directions, and the ellipticity of the point spread function (PSF) was used to locate the position of particles in the z axis. The z calibration curve was obtained by recording the change of the widths of the PSF in the x and y direction. The calibration sample was prepared using 1 mL of a dilute FMSN(+) solution (2.5 μg/mL) drop-casted on a coverslip. The sample was then scanned in the z direction with a step size of 20 nm. The images of individual particles were then fitted to an elliptical Gaussian function to obtain the widths in the x and y directions.

pH Calibration

To establish the pH calibration curve, FMSNs (2.5 μg/mL) were first dispersed in phosphate buffered solution (ionic strength = 0.05 M) at a known pH (in the range between 3.5 and 7.5), and 1 mL of each mixture was dropped on a coverslip. The microscope was focused in a plane right on the coverslip, and with the same settings (*e.g.*, laser power, gain, exposure time and resolution) employed for the single particle tracking experiments. More than 50 bright fluorescence particales were collected at each pH value and used to obtain the fluorescent intensity ratio of FITC and RITC. The pH calibration curve was obtained by fitting the data with a sigmoidal function.

Cell Culture

HeLa cells, human cervical carcinoma cells, were maintained in Dulbecco's modified Eagles medium (DMEM; GIBCO), 10% fetal ovine serum (FBS; GIBCO) and 1% antibiotics (100 U/mL penicillin and 100 μg/mL streptomycin; GIBCO). The HeLa cells were incubated at 37 °C under a humidified atmosphere of 95% air and 5% CO_2. When adherent cells reached ~ 60% to 70% confluence, they were detached with 0.25% trypsin-EDTA growth medium to allow for continued passaging. Details are given in supporting information.

Single Particle Tracking and Spectroscopy in Live Cell

HeLa cells were cultured on an 18 mm diameter glass coverslip one day prior to the tracking experiments. Cells on the coverslips were cultured in growth medium in 6-well Nunc™ Cell-Culture Treated Multidishes (Thermo) at 37 ℃ in a 95% air and 5% CO_2 atmosphere. Before the experiment, HeLa cells were washed three times with 1 mL DMEM (without serum and phenol red). Then, 1 mL of FMSNs (2 μg/mL) contained DMEM (without serum and phenol red) solution was added and incubated at 37 ℃ in a 95% air and 5% CO_2 environment for 10 min/ 2 h/ 4 h. Then, the supernatants were removed and cells were washed three times with PBS, and kept in PBS for observation.

Drug Treatment

To study the variation of the cellular endocytic process when the cell was evolving into a dysfunction form, 1 mL of methyl viologen hydrate (paraquat) aqueous solution (75 mM, keep in 37 °C) was added into the sample by syringe without disturbing the temperature and air composition in the incubator. Paraquat is well-known for causing cellular apoptosis via generating free radicals.

Results and discussion

Dual-emissive FMSNs are synthesized by the co-condensation of (3-Aminopropyl)trimethoxysilane (APTMS)-conjugated FITC and APTMS-conjugated RITC with a cationic surfactant cetyltrimethylammonium bromide (CTAB) and tetraethyl orthosilicate (TEOS)/ethanol/water solution system. The design of MSN-based pH sensor is illustrated in Figure 1a. Because of its

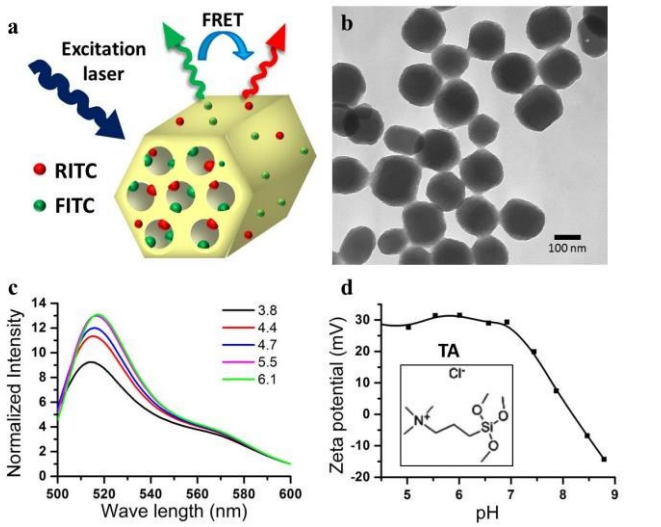

Figure 1: Design and characterization of FMSN(+). (a) Schematic of FMSN(+) and the RITC dyes can be excited though FRET effect or direct excitation when being excited by a single wavelength laser. (b) TEM image. (c) Fluorescence spectrum of FMSNs(+) in buffered solutions with different pH obtained from a fluorescence spectrophotometer . The wavelength of excitation is 473 nm. (d) Zeta potential plot and the structural formula of TA. FMSNs(+) are dispersed in water for measurement.

mesostructure, confined dye molecules are prevented from aggregation and photo-degradation.[49] In order to improve cellular uptake, the as-synthesized FMSNs are modified with a trimethylammonium group (TA) on their surfaces to possess positive charges (FMSN(+)). The average diameter of the FMSN(+) was measured to be 150 nm based on the TEM images as shown in Figure 1b; and the hydrodynamic diameter was estimated by dynamic light scattering to be about 200 nm (Figure S1a). The photo-luminescence spectra of FMSNs(+) at different pHs (Figure 1c) revealed that the emission ratios of FITC and RITC changed significantly with the environmental pH. Zeta potential of FMSN(+) indicated that the TA was successfully modified onto the surfaces of the FMSNs, leading to high positive surface charge when the surrounding pH was below 8 (Figure 1d). The XRD pattern showed three diffraction peaks approximately 2θ = 2.0, 4.0 and 4.5 characteristic of hexagonal symmetry, indicating a highly ordered mesoporous structure (Figure S1b). The capillary condensation was

observed at a relative pressure P/P_0 between 0.2 and 0.25 in typical type IV nitrogen adsorption-desorption isotherms (Figure S2a), showing the existence of mesoporous channels. A surface area of 649.2 m^2/g was obtained by BET (Brunauer – Emmett – Teller) analysis and the pore size and pore volume were calculated to be 1.9 nm and 0.663 cm^3/g, respectively by Barrett-Joynrt-Halenda (BJH) analysis.

The wide-field imaging based 3D single-particle-tracking system is depicted in Figure 2a. As shown in Figure 2b, the widths of the PSF of FMSN(+) in the x and y directions obtained from a 2D Gaussian fitting were recorded when the objective was scanned along the z axis. With this z calibration curve, one can determine the location of the particle in the z direction according to the shape of PSF.(Examples of shape of PSF is shown in Fig. S3) To estimate the accuracy of the location assignment, FMSNs(+) were deposited onto the surface of a cover glass and two thousand frames were collected over a period of 5 minutes. As shown in Figure 2d, the accuracies (standard deviations) in the x, y and z axes are 5, 7.5, 13.5 nm, respectively, which are comparable with the previously reported values in single-particle tracking techniques.[28, 29, 31, 44] The large number of dyes within a single MSN makes it bright and the localization of position accurate. The pH calibration curve, shown in Figure 2c, was determined using the emission intensity ratio (EIR) of FITC/RITC contributed from FMSNs(+) at different pH values. At each pH, the EIRs from more than 50 FMSN(+)s were averaged.

Before applying FMSN(+) in the intracellular studies, various control experiments were performed.[50] Under continuous photo-excitation, the emissive intensities of FITC and RITC decayed because of photo-bleaching (7 nanoparticles examples are given in Figure S4a), but the EIR remained nearly constant for the duration of the photo-stability test (1 frame per 15 s for one hour), indicating that the FMSNs can be reliably used for long-term pH sensing (Figure S4b). As shown in Figure S5a, FMSNs(+) exhibited great reproducibility across three pH cycles, and we demonstrated that the response of the FMSNs(+) was fast when altering the environmental pH between extreme values (each cycle occurred over 20 seconds), as shown in Figure S5b. Moreover, the EIR of FMSNs(+) exhibited a stable value at different excitation laser powers, from 0.5 μW to 3 μW (Figure S6), suggesting that the readout was not affected by fluctuations of excitation light source. To observe changes in intracellular pH, we usually performed the single particle tracking experiments for about twenty minutes; thus the stability of the microscope stage was crucial. To test x, y and z drift (Figure S7) we immobilized FMSN(+) onto the surface of cover glass

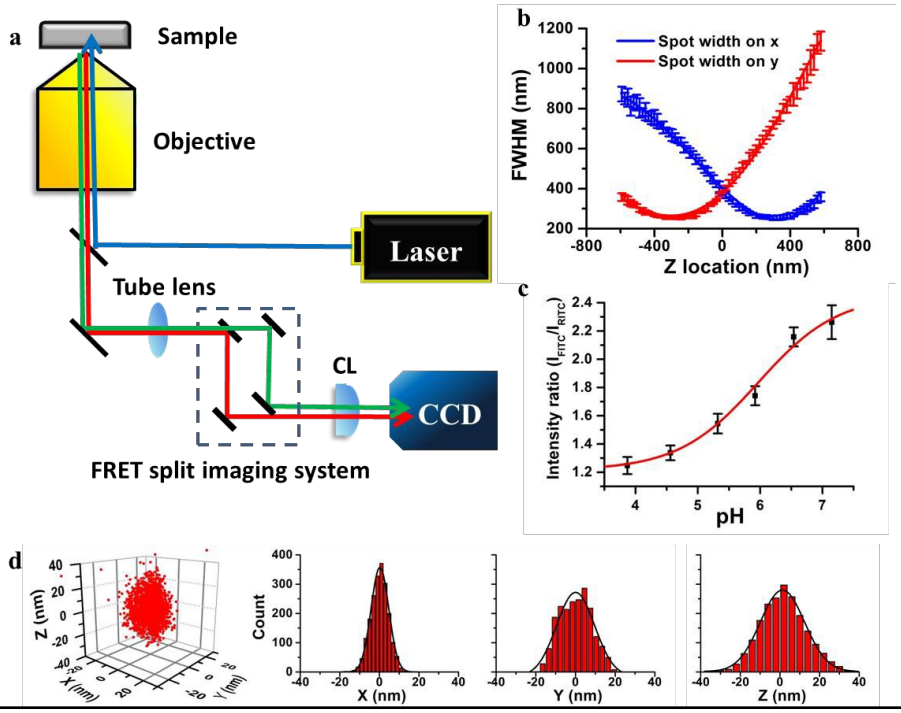

Figure 2: (a) Scheme of the 3D single particle tracking apparatus. CL: cylindrical lens. (b) The z calibration curve of full width at half maximum (FWHM) of fitted images in the x and y direction as a function of z obtained from ten FMSNs(+). The images of individual particles are then fitted to an elliptical Gaussian function. Mean±SD is represented. (c) The pH calibration curve of a FMSN(+). For each pH, more than 50 single particles are used in calculation. Mean±SD is represented. (d) Three dimensional localization distribution of a FMSN(+). Histograms of the distribution in x, y and z are fitted to a Gaussian function, yielding standard deviations of 5 nm in x, 7.5 nm in y and 13.5 nm in z.

and tracked the position of a particle for one hour (1 frame per 15 s). Although the direction of drift was random, the displacements in all directions within one hour were less than 50 nm, and the average root-mean-squared (RMS) speed was lower than 1.5 nm/s (Figure S8), indicating that the random x, y and z drift during a twenty-minute-tracking experiment was a minor concern. The precision of pH detection was poor when fluorescence intensity of FMSN(+) was low (Figure S9), as insufficient intensity leads to bigger fluctuations in the EIR readout. With an ample photon budget, the FMSN(+) pH reporter afforded to report pH value with the precision better 0.3 pH unit. Therefore, a powerful pH probe with an ample photon budget and great photo-stability is also a key factor for reliably monitoring the intracellular pH.

In order to obtain a correlation between the local pH variation and the movement of the particles at different endocytosis stages, the investigation was divided into three time zones, 10 min, 2 hrs and 4 hrs after the incubation of the cells with the fluorescent probes. The speed, pH, and trajectories were extracted and classified to obtain a more detailed model of endocytosis. To confirm that the pH readout was stable even after

a long time, we determined the pH calibration curves of FMSNs(+) in phosphate buffer solutions at 10 minutes and 6 hours after suspension (Figure S10). To verify that the FMSNs(+) were located in the cells, the membrane of HeLa cells were stained with FM4-64 after tracking. The emission from FM4-64 was collected in the RITC channel (Figure S11). A representative result of a 10-min tracking (one frame per 5 s) is shown in Figure 3. The FMSNs(+) are located near the cell membrane, as shown in Figure 3a, and the trajectory indicates that that displacements in the x and z directions are limited to a small range, shown in Figure 3b. The fluorescent intensities of FITC and RITC and the corresponding pH throughout the duration of the experiment are shown in Figure 3c. According to the change in the FITC/RITC intensity ratio, the local pH changes from neutral to weakly

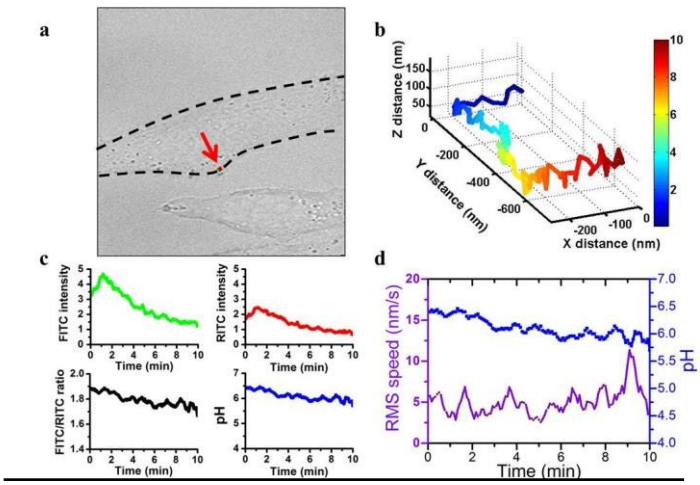

Figure 3: The trajectory and fluorescent intensity of a representative FMSN(+) after 10 min incubation with HeLa cells (one frame per 10 s, tracking for 20 min). (a) The bright field image combined with the trajectory of the FMSN(+). (b) The trajectory of the FMSN(+). The color bar represents tracking time (min), giving that the path starts from blue and ends in red. (c) Plots of the FITC and RITC intensities, the FITC/RITC ratio and the local pH. (d) Plots of the local pH and root mean square speed.

acidic, indicating acidification similar to that in the early endocytic process. To study the correlation between the motion of FMSNs(+) and changes in local pH, the time-dependent pH plots and the RMS speed plots are overlaid, as shown in Figure 3d. These results suggest FMSNs(+) are confined within an acidic endosome after a 10-min incubation. For the case of 2 hours incubation (a representative result shown in Figure S12), the displacement is also limited to a 10 min window, the results were similar to that observed in the 10-min tracking result.

After 4-hour incubation, there were many trajectories that exhibited fast moving FMSNs and basification, these behaviors were quite different from the results observed at 10-min and 2-hour incubations (a representative result from these special cases is shown in Figure S13). Based on these results, we deduced that these FMSNs(+) were trapped in an acidifying endosome at early times, and then they undergo an endosomal escape process, which was observed as basification and fast movement at the same time. To verify our assumption, it is necessary to collect statistically significant number of trajectories at a different incubation time.

We classify the trajectories into four types in terms of their pH changes with respect to time. For the tracked FMSNs(+), initial time-dependent pH plots are fitted with a straight line. Representative types according to pH plots are shown in Figure 4. The pH variation types are classified as type A (acidification) or type B (basification) when the slopes were lower than -0.017 or higher than 0.017 (pH/min), respectively. It is called type N when there is no obvious pH change, meaning the slope is between -0.017 and 0.017 (pH/min). There are, however, a fourth type exhibiting basification and then saturation at neutral pH; these are categorized as type B2. For B2 type, the whole data set is fitted with a sigmoidal function in green, and the early basification part is fitted with a straight line in red, as shown in Figure 4d.

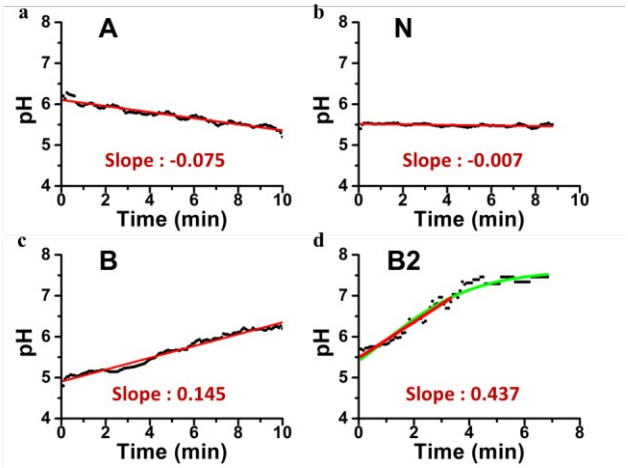

Figure 4: Typical cases of four types of observed pH trends. (a) Type A. (b) Type N. (c) Type B. (d) Type B2. The classification of pH trend type was decided by the slope of fitting curve in pH plot, slope < -0.017 (pH/min) is defined as type A; -0.017 < slope < 0.017 is defined as type N; slope > 0.017 (pH/min) is defined as type B. In some special cases, the pH increases to a limiting value, which cannot be fitted by a line. These cases are defined as type B2.

The statistical results of the slope in pH variation and type, and the average RMS speed are shown in Figure 5. After 10-min and 2-hour incubation, the fitted slopes of pH changes are negative in more than half of the cases indicating that acidification occurred in early endocytosis of the FMSNs(+). The same trend can also be observed in the pie charts categorizing the types of time-dependence of the pH variation, shown in Figure 5b. The pie charts indicate that more basification is observed after a 2-hour and 4-hour incubation of FMSN(+), and more type B2 pH variations are observed after 4-hour incubation. The distribution of the average RMS speed is broader and shifted to higher speed after 2-hour and 4-hour incubations than that after 10-min incubation as shown in Figure 5c. Based on the statistics, it suggests that the FMSNs(+) were confined in acidifying endosomes at early times, and then the FMSN(+) started to move out from the confined volume, resulting in basification, which is consistent with the assumption of endosome escape. We also analyzed the pH distribution after different incubation time, (shown in Figure S14). The process of endosome turning into lysosome takes time and the pH in lysosome is about 4.5. Based on our results in Figure S14, there is no nanoparticle in the pH 4.5 range until 4h incubation. Therefore, we believe that in the early stage of endocytosis, most particles are trapped in endosomes rather than lysosomes.

In addition to categorizing the results by incubation time, we

further classified the data by type of pH variation. Both type A and type B show wide distributions of the pH values (Figure S15a), and these results are expected because the pH variation is large during acidification and basification. Owing to the saturating nature of the type B2 pH variations, the average pH values are around neutral pH (Figure S15a). Surprisingly, most of the average pH values of the type N variations are near a pH of ~5.5, implying that this pH value may be the lowest value during the endocytosis process of FMSN(+) (Figure S15a). In addition to the average pH, the RMS speeds of the FMSNs also contain interesting results. All of the type-A FMSNs(+) have low average RMS speed, and most of the type-B and type-B2 FMSNs(+) have much faster average RMS speeds. Interestingly, the distribution of the average RMS speed of the type-N FMSNs(+) is divided into two parts: one group has an average RMS speed of approximately 5 nm/s and the others have a much faster speed as did the type-B or type-B2 FMSNs(+) (Figure S15b).

To understand the diverse movement of type-N FMSNs(+), we further analyzed the correlation of both the average pH and the average speed vs. the incubation time in the type N particles, shown in Figure S16. Most of the FMSNs after the 10-min and 2-hour incubations exhibited a low average pH (~5.5) and a low RMS speed with behaviors that were similar to the type-A FMSNs(+). This result implies that this group of type-N FMSNs(+) reached their lowest pH value during their endocytic process. The type-N FMSNs(+) after the 4-hour incubation exhibit a broad distribution of the average pH and RMS speed. These results are similar to the static results of the type-B FMSNs(+), suggesting that this group of type-N FMSNs(+) may be involved the same process as the type-B FMSNs(+), but the fitted slope is not high enough to be classified as a type-B FMSN(+).

In order to have better understanding of the correlation between the pH variation and RMS speed of a FMSN(+) during both the endocytic and exocytic processes, a plot of the fitted pH slope vs. the average RMS speed for a given incubation time is shown in Figure 6. This plot clearly indicates that the FMSNs(+) are kept at low speed during acidification, implying the FMSNs(+) are well-confined in the endosome. Conversely, the FMSNs(+) have more mobility during basification, including type B and B2, implying the FMSNs(+) are moving out from endosome to cytosol. As discussed previously, there are two groups of distributions found in the type-N FMSNs(+), which can be assigned as two extreme cases: FMSNs(+) that are well-confined in endosomes and those already free to move out of the endosome.

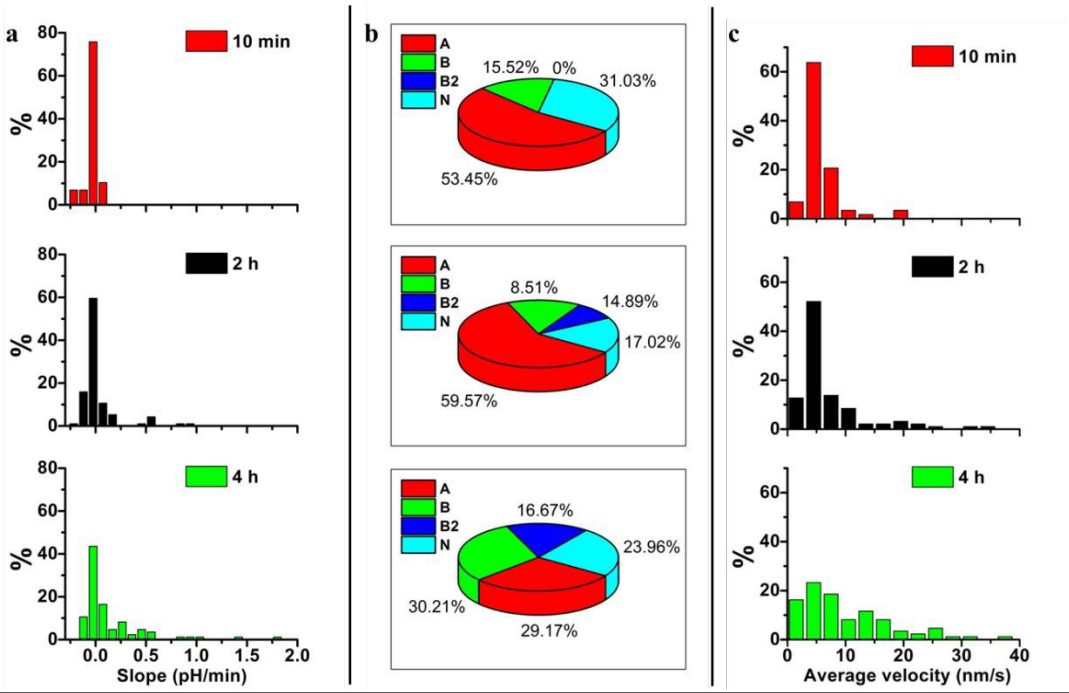

Figure 5: Distributions of the FMSNs(+) separated by their incubation times. (a) Slopes from the fitted pH curves (b) pH variation types (c) Average velocities. The total numbers of FMSN(+) employed in 10 min, 2 h and 4 h incubation analysis were 58, 94 and 86 respectively.

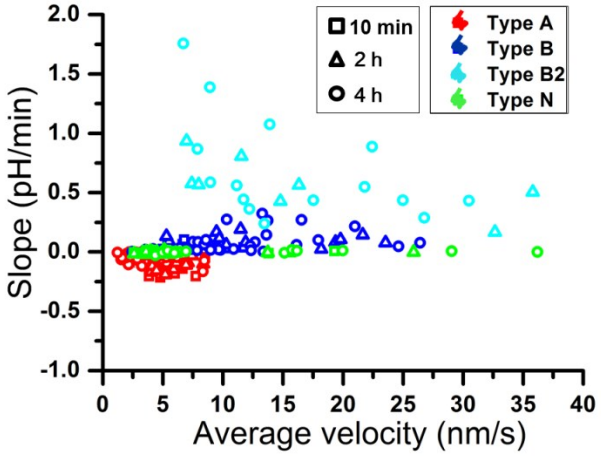

Figure 6: Plot of the slope from the fitted curves and the corresponding average velocity of each of the pH variation types. The slope of the type B2 particles refers to the slope of the curve before saturation.

According to the statistical analysis, the pH variation of the type B2 particles is always accompanied by a high speed movement. In the early discussion, this behavior was assigned as endosomal escape (moving out from endosome). Endosome escape may not be the only cause of basification and high mobility at later time. In some type-B2 cases, we observed cell morphology changes, as shown in S17a and b, which may be an additional source of fast moving FMSN(+). Cell morphology changes are considered to be an indicator of cell dysfunction or apoptosis. This consequence may be reasonable considering no nutrition is provided after incubation with FMSNs(+). To verify cell dysfunction or apoptosis will lead the escape of the FMSNs(+) from the endosomes, paraquat (a chemical that can induce cell apoptosis) was added to samples after a 1-hour incubation with FMSNs(+). Type B2 behavior was reproduced, as shown in Figure S17 and Figure S18 (two independent cases), supporting the augment that cell dysfunction or apoptosis leads to fast moving FMSN(+).

3D-SPT and ratiometric pH detection measurements allowed us to extract important information during the endocytosis and exocytosis of FMSN(+) in HeLa cells. We summarize the endocytic process of FMSN(+) in HeLa cell with three separated stages (Figure 7). At first, we observe acidification and slow movement of the FMSNs(+) (type A and type N), which is assumed to be FMSNs(+) confined in endosomes. This observation mostly occurs after 10 min of incubations. Before FMSN(+) can totally escape from the endosome, an intermediate state with fast speed and basification is observed (type B), suggesting an expansion of the endosome via the inflow of cytosol is occurring. The likelihood of basification significantly increases with incubation time. Finally, FMSN(+) is able to escape from the endosome to the cytosol with a neutral local pH and a faster RMS speed (type B2 and type N). However, it is important to note that this result may be simply due to cell dysfunction because no nutrition was provided during data collection. The lower pH boundary used in this study was ~5.5, implying that the FMSN(+) endocytic pathway in HeLa cells may not reach late endosomes or lysosomes. The statistical analysis and proposed model are important information that may be useful when designing a TA-passivated FMSN for drug delivery and release.

To understand the influence of FMSN's surface charge on the endocytic process, we synthesized similar dual dye-loaded FMSNs that were negatively charged via 3-trihydroxysilypropylmethylphosphonate (THPMP) grafted onto the FMSN surfaces (details are elucidated in SI). The TEM image, XRD pattern, pH-dependent FL spectra and Zeta potential of FMSN(-) are shown in Figure S19, which shows similar results to the FMSNs(+) except for the the Zeta potential. 3D-SPT and pH detection were performed using the same method. The statistical results of the average pH, pH variation type and average RMS speed classified by the incubation time were analyzed, and the results are shown in Figure S20. Unlike the FMSNs(+), the average pH distributions shifted to lower pH more slowly and ended up at a lower final pH value, shown in Figure S20a. In addition, the type A behavior was observed as the dominant type in every incubation time, shown in Figure S20b. Furthermore, the RMS speed distributions of FMSN(-) was keep to lower speeds at different incubation times, shown in Figure 20c, implying that most of the negatively charged FMSN(-) particles were trapped in the endosome.

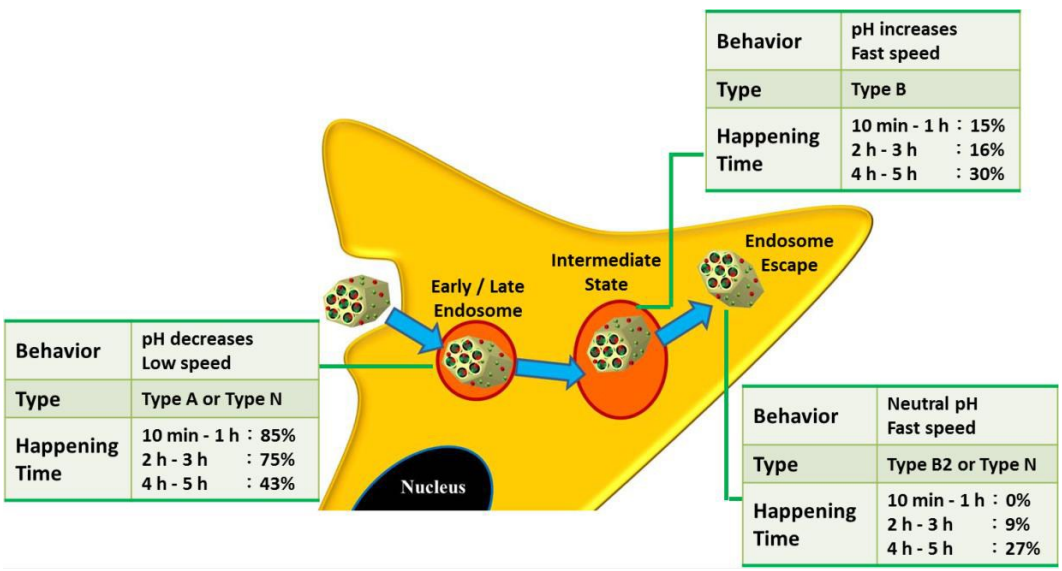

Figure 7: The proposed model of the endocytic pathway of FMSN(+).

Conclusions

We combined ratiometric sensing and 3D single-particle tracking techniques to investigate the trafficking of a single nanoparticle (FMSN) and its surrounding pH changes during an endocytic process in HeLa cell. The versatility of the FMSNs is the key to achieve this measurement because of their stability and high brightness, allowing stable and reliable ratiometric pH sensing and 3D single-particle tracking. The precision of pH detection (~0.3 pH unit) and that of 3D localization (~10 nm) achieved in this study are state-of-art pH sensing and 3D single-particle tracking in living cells, if separately compared. With this nanoparticle system, we observed that the FMSNs underwent acidification with a lower mobility at the early stage of the endocytosis process. At the late stage of the endocytosis process, the basification of microenvironment around the FMSNs occurred with higher mobility. It is possible to trace the evolution of local pH values around an FMSN dynamically during the endocytosis process with this system. Considering the multi-functionality and tunability of FMSNs and the flexibility of the modified wide-field microscope, this combination of FMSNs and a 3D-SPT system can be further modified to study trafficking and sensing local environment other than the pH value in living cells. Molecular sensing capability such as Ca^{2+} ion or H_2O_2 may be built into the nanopores of FMSN.[51, 52] One can expect to provide the detailed intracellular trafficking information to develop a new generation of smart nanoparticles for biomedical applications.

Acknowledgements

This research was funded by the Ministry of Science and Technology (MOST) of Taiwan. P. Chen would like to thank the financial support from the MOST of Taiwan under contract MOST 103-2113-M-001-008-MY3, NSC-101-2120-M-001-011 and the Academia Sinica Research Project on Nano Science and Technology.

References

1. J. L. Vivero-Escoto, R. C. Huxford-Phillips and W. Lin, *Chem. Soc. Rev.*, 2012, **41**, 2673.
2. P. Yang, S. Gai and J. Lin, *Chem. Soc. Rev.*, 2012, **41**, 3679.
3. S.-H. Wu, Y. Hung and C.-Y. Mou, *Chem. Commun.*, 2011, **47**, 9972.
4. Q. He and J. Shi, *Advanced Materials*, 2014, **26**, 391.
5. Y.-S. Lin, C.-P. Tsai, H.-Y. Huang, C.-T. Kuo, Y. Hung, D.-M. Huang, Y.-C. Chen and C.-Y. Mou, *Chem. Mater.*, 2005, **17**, 4570.
6. Y.-S. Lin, S.-H. Wu, Y. Hung, Y.-H. Chou, C. Chang, M.-L. Lin, C.-P. Tsai and C.-Y. Mou, *Chem. Mater.*, 2006, **18**, 5170.
7. D. Tarn, C. E. Ashley, M. Xue, E. C. Carnes, J. I. Zink and C. J. Brinker, *Acc. Chem. Res.*, 2013, **46**, 792.
8. F. Lu, S.-H. Wu, Y. Hung and C.-Y. Mou, *Small*, 2009, **5**, 1408.
9. F. Zhao, Y. Zhao, Y. Liu, X. Chang, C. Chen and Y. Zhao, *Small*, 2011, **7**, 1322.
10. J.-K. Hsiao, C.-P. Tsai, T.-H. Chung, Y. Hung, M. Yao, H.-M. Liu, C.-Y. Mou, C.-S. Yang, Y.-C. Chen and D.-M. Huang, *Small*, 2008, **4**, 1445.
11. K. Welsher and H. Yang, *Nat. Nano*, 2014, **9**, 198.
12. P. Sandin, L. W. Fitzpatrick, J. C. Simpson and K. A. Dawson, *ACS Nano*, 2012, **6**, 1513.
13. D. Lißе, C. P. Richter, C. Drees, O. Birkholz, C. You, E. Rampazzo and J. Piehler, *Nano Lett.*, 2014, **14**, 2189.
14. Y. W. Cho, J.-D. Kim and K. Park, *J. Pharm. Pharmacol.*, 2003, **55**, 721.
15. H. Yuan, A. M. Fales and T. Vo-Dinh, *J. Am. Chem. Soc.*, 2012, **134**, 11358.
16. Y.-P. Chen, C.-T. Chen, Y. Hung, C.-M. Chou, T.-P. Liu, M.-R. Liang, C.-T. Chen and C.-Y. Mou, *J. Am. Chem. Soc.*, 2013, **135**, 1516.
17. J.-P. Behr, *CHIMIA Int. J. Chem.*, 1997, **51**, 34.
18. T. F. Martens, K. Remaut, J. Demeester, S. C. De Smedt and K. Braeckmans, *Nano Today*, 2014, **9**, 344.
19. A. K. Varkouhi, M. Scholte, G. Storm and H. J. Haisma, *J. Controlled Release*, 2011, **151**, 220.
20. A. Burns, P. Sengupta, T. Zedayko, B. Baird and U. Wiesner, *Small*, 2006, **2**, 723.
21. L. Wang, J. Lei and J. Zhang, *Chem. Commun.*, 2009, 2195.
22. R. V. Benjaminsen, H. Sun, J. R. Henriksen, N. M. Christensen, K. Almdal and T. L. Andresen, *ACS Nano*, 2011, **5**, 5864.
23. M. J. Marín, F. Galindo, P. Thomas and D. A. Russell, *Angew. Chem. Int. Ed.*, 2012, **51**, 9657.
24. X. D. Wang, J. A. Stolwijk, T. Lang, M. Sperber, R. J. Meier, J. Wegener and O. S. Wolfbeis, *J. Am. Chem. Soc.*, 2012, **134**, 17011.
25. L. Yin, C. He, C. Huang, W. Zhu, X. Wang, Y. Xu and X. Qian, *Chem. Commun.*, 2012, **48**, 4486.
26. J. Lei, L. Wang and J. Zhang, *Chem. Commun.*, 2010, **46**, 8445.
27. Y.-P. Chen, H.-A. Chen, Y. Hung, F.-C. Chien, P. Chen and C.-Y. Mou, *RSC Adv.*, 2012, **2**, 968.
28. C.-J. Tsou, C.-y. Chu, Y. Hung and C.-Y. Mou, *J. Mater. Chem. B*, 2013, **1**, 5557.
29. S. H. Wu, Y. Hung and C. Y. Mou, *Chem. Commun.*, 2011, **47**, 9972.
30. C.-H. Lee, T.-S. Lin and C.-Y. Mou, *Nano Today*, 2009, **4**, 165.
31. A. M. Dennis, W. J. Rhee, D. Sotto, S. N. Dublin and G. Bao, *ACS Nano*, 2012, **6**, 2917.
32. T. Doussineau, A. Schulz, A. Lapresta-Fernandez, A. Moro, S. Körsten, S. Trupp and G. J. Mohr, *Chem. Eur. J.*, 2010, **16**, 10290.
33. H. S. Peng, J. A. Stolwijk, L. N. Sun, J. Wegener and O. S. Wolfbeis, *Angew. Chem. Int. Ed.*, 2010, **49**, 4246.
34. D. Montiel and H. Yang, *Laser & Photonics Reviews*, 2010, **4**, 374.
35. M. J. Saxton and K. Jacobson, *Annu. Rev. Biophys. Biomol. Struct.*, 1997, **26**, 373.
36. N. P. Wells, G. A. Lessard, P. M. Goodwin, M. E. Phipps, P. J. Cutler, D. S. Lidke, B. S. Wilson and J. H. Werner, *Nano Lett.*, 2010, **10**, 4732.
37. N. F. Reuel, A. Dupont, O. Thouvenin, D. C. Lamb and M. S. Strano, *ACS Nano*, 2012, **6**, 5420.
38. K. McHale, A. J. Berglund and H. Mabuchi, *Nano Lett.*, 2007, **7**, 3535.
39. M. F. Juette and J. Bewersdorf, *Nano Lett.*, 2010, **10**, 4657.
40. J. J. Han, C. Kiss, A. R. M. Bradbury and J. H. Werner, *ACS Nano*, 2012, **6**, 8922.
41. H. P. Kao and A. S. Verkman, *Biophys. J.*, 1994, **67**, 1291.
42. J..Gelles, B.J. Schnapp, M.P. Sheetz, *Nature*, 1988, **331**, 450
43. E. Toprak, H. Balci, B. H. Blehm and P. R. Selvin, *Nano Lett.*, 2007, **7**, 2043.
44. B. Huang, W. Wang, M. Bates and X. Zhuang, *Science*, 2008, **319**, 810.
45. Y. Li, Y. Hu and H. Cang, *J.f Phys. Chem. B*, 2013, **117**, 15503.
46. A. Huefner, D. Septiadi, B. D. Wilts, I. I. Patel, W.-L. Kuan, A. Fragniere, R. A. Barker and S. Mahajan, *Methods*, 2014, **68**, 354.
47. L. Liang, J. Li, Q. Li, Q. Huang, J. Shi, H. Yan and C. Fan, *Angew. Chem. Int. Ed.*, 2014, **53**, 7745.
48. C. H. Jones, C.-K. Chen, A. Ravikrishnan, S. Rane and B. A. Pfeifer, *Mol. Pharm.*, 2013, **10**, 4082.
49. B. Biermann, S. Sokoll, J. Klueva, M. Missler, J. S. Wiegert, J. B. Sibarita and M. Heine, *Nat. Commun.*, 2014, **5**, 1-10.
50. S. Chang, X. Wu, Y. Li, D. Niu, Y. Gao, Z. Ma, J. Gu, W. Zhao, W. Zhu, H. Tian and J. Shi, *Biomaterials*, 2013, **34**, 10182.

51. E. Zagato, K. Forier, T. Martens, K. Neyts, J. Demeester, S. D. Smedt, K. Remaut and K. Braeckmans, *Nanomedicine*, 2014, **9**, 913.
52. D. Vercauteren, H. Deschout, K. Remaut, J. F. J. Engbersen, A. T. Jones, J. Demeester, S. C. De Smedt and K. Braeckmans, *ACS Nano*, 2011, **5**, 7874.